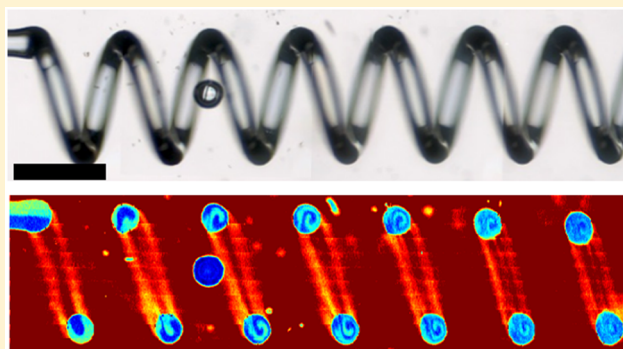


Quantitative Chemical Imaging of Nonplanar Microfluidics

Matthew K. Gelber,^{†,‡} Matthew R. Kole,^{†,‡} Namjung Kim,^{†,§} Narayana R. Aluru,^{†,§}
and Rohit Bhargava^{*,†,‡,§,||} [†]Beckman Institute for Advanced Science and Technology, [‡]Department of Bioengineering, [§]Department of Mechanical Science and Engineering, and ^{||}Departments of Electrical & Computer Engineering, Chemical and Biomolecular Engineering and Chemistry, University of Illinois, Urbana, Illinois 61801, United States Supporting Information

ABSTRACT: Confocal and multiphoton optical imaging techniques have been powerful tools for evaluating the performance of and monitoring experiments within microfluidic devices, but this application suffers from two pitfalls. The first is that obtaining the necessary imaging contrast often requires the introduction of an optical label which can potentially change the behavior of the system. The emerging analytical technique stimulated Raman scattering (SRS) microscopy promises a solution, as it can rapidly measure 3D concentration maps based on vibrational spectra, label-free; however, when using any optical imaging technique, including SRS, there is an additional problem of optical aberration due to refractive index mismatch between the fluid and the device walls. New approaches such as 3D printing are extending the range of materials from which microfluidic devices can be fabricated; thus, the problem of aberration can be obviated simply by selecting a chip material that matches the refractive index of the desired fluid. To demonstrate complete chemical imaging of a geometrically complex device, we first use sacrificial molding of a freeform 3D printed template to create a round-channel, 3D helical micromixer in a low-refractive-index polymer. We then use SRS to image the mixing of aqueous glucose and salt solutions throughout the entire helix volume. This fabrication approach enables truly nonperturbative 3D chemical imaging with low aberration, and the concentration profiles measured within the device agree closely with numerical simulations.



Microfluidic devices allow precise management of small quantities of material, allowing control and observation of chemical, biological, and physical phenomena.¹ Integral to their use are microscopy technologies, including optical coherence tomography,² confocal fluorescence,^{3,4} 2-photon fluorescence,⁵ spontaneous confocal Raman spectroscopy,^{4,6} and coherent anti-Stokes Raman spectroscopy (CARS).^{7,8} Raman microscopy is particularly attractive because it eliminates the need for exogenous labels, which may disrupt the native transport properties or other behaviors of the species of interest in small microfluidic volumes. While the long acquisition times required for weak spontaneous Raman signals made its use prohibitive, emerging coherent two-photon Raman microscopies now offer a fast alternative. Stimulated Raman scattering (SRS) microscopy,⁹ in particular, can enable quantitative imaging without the nonspecific background effects and nonlinear analyte response seen in CARS. One challenge all techniques face is the limiting effect of optical distortion caused by the microfluidic device features on quantitative accuracy of the measurement. The microfluidic device's interfaces introduce spherical aberration and affect the effective depth to which the beam(s) focuses, the confocal volume changes as a function of depth, and a reduced collection efficiency often results, leading to “dark” or “hidden” regions

within the image.^{10–12} Curved surfaces can additionally introduce lensing effects. The specific relationship between channel position and optical aberration depends on the channel depth, the numerical aperture of the illumination/collection optics, the refractive indices of the chip material and the fluid, and the shape of the interface (Figure 1a), making quantitative measurements difficult. For wide, shallow channels with a flat surface perpendicular to the optical axis, changes in image quality across the device tend to be small and can be corrected for¹³ or neglected.^{14,15} However, for narrow, deep channels or channels with curved walls, images can be severely distorted. This is quite obvious in SRS images of a channel with a round cross section (Figure 1b), and similar aberrations are apparent in confocal fluorescence microscopy of round cross section, helical channels^{16,17} of a fused silica device. While novel optics have been used to correct for simple cases,¹⁸ functional devices can often be sufficiently complex to render this approach impractical. Recent advances in microfabrication are resulting in complex, nonplanar 3D channels and intricate microfluidic devices that are especially attractive for a wide range of needs,

Received: October 7, 2016

Accepted: December 16, 2016

Published: December 16, 2016

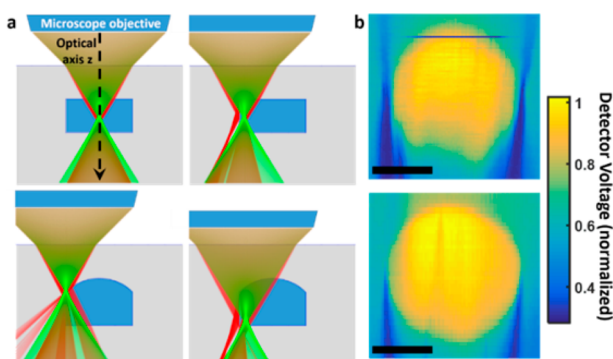


Figure 1. Aberrations in microfluidic devices do not permit straightforward imaging. (a) Ray-tracing simulation indicating how the features of a microfluidic channel can distort the focal volume of a confocal/multiphoton imaging technique. Red rays assume a glass (NBK-7) device and a water-filled channel, while green rays assume the device material has been matched to the refractive index of water. While spherical aberrations are induced by the air–device interface, the majority of issues occur from device features. (b) Top: SRS image of a cross section of a circular microfluidic channel without refractive index matching (device and fluid are 1.565 and 1.376, respectively). The channel cannot be resolved. The horizontal line of dark pixels at the top of the channel is due to a bubble, which flowed through the channel while those pixels were acquired. Bottom: The fluid has been changed to RI 1.518, reducing but not eliminating the mismatch between the two components. The cross section is fully resolved, and “dark” regions are significantly reduced. Scale bar = 100 μm .

from sophisticated mimicking of physiologic systems¹⁹ to making practical elastomeric valves that completely seal.²⁰ For example, round channels are required to mimic physiological channel networks, including blood vessels^{21–24} and the secretory duct networks in the breast²⁵ and prostate.²⁶ Round channels also have a minimal ratio of surface area to volume, which minimizes the rate of fouling, the pressure required to push a bubble through the channel,²⁷ and the pressure drop due to viscous losses. However, optical imaging of such structures is complicated, and there are no studies to demonstrate that microscopic phenomena can be accurately measured with high fidelity.

Here we sought to develop an approach to make high-fidelity measurements in nonplanar microfluidic devices using non-perturbative two-photon SRS microscopy. We first make use of a versatile approach to fabricate complex, round-channel microfluidics that is emerging via the use of 3D printing.^{28–33} This method involves the fabrication of a sacrificial template, around which a curable material is cast. Realizing that this casting method is compatible with a wide range of curable materials permitting a wide range of refractive indices, our method matches the refractive index of the chip itself to the fluid in the channels. Eliminating refractive index mismatch-dependent aberrations throughout the device permits imaging without adaptive optics or computation even for complex geometries. The ability to fabricate and image these complex geometries opens a new design space for solving many problems in microfluidics, including classical problems such as mixing in the laminar flow regime. To demonstrate this, we use the sacrificial molding approach to fabricate a helical micromixer. In a helical or Dean-effect micromixer, centripetal acceleration of fluid flowing around a curve creates vortices that rotate transversely to the direction of flow. These Dean vortices can be used to fold the interface between two adjacent fluid

elements, increasing the interfacial area and diffusive transport between them.³⁴ The magnitude of this effect is related to the Dean number, which is given by

$$De = Re \sqrt{\frac{r}{R}} = \frac{2Q}{\nu\pi} \sqrt{\frac{1}{rR}}$$

where Re is the Reynolds number, Q is the mass flow rate, ν is the kinematic viscosity, r is the radius of the channel cross section, and R is the radius of curvature. Physically, De represents the ratio of centripetal forces to viscous forces, and vortex-induced folding of the fluid interface becomes significant when De is on the order of 1. Though modeling^{16,35–37} and some experimental^{16,38} results indicate that helical designs can create effective passive micromixing devices, there has been no direct comparison of the predicted mixing profile with experiment, and no comparison of the performance with that of more conventional mixers fabricated via soft lithography. Hence, we use SRS microscopy to directly measure chemical distributions of a dissolved species and quantify mixing. Numerical modeling is used to validate both the imaging results as well as our design principle and to help understand the mixing process in these devices. The agreement between experimental and theoretical profiles will demonstrate the fidelity of the fabrication process as well as the accuracy of visualization using chemical imaging.

RESULTS

Device Fabrication. An overview of the sacrificial template process used and microfluidic mixers made in this study is shown in Figure 2. Our approach to manufacturing these devices consists of three steps (Figure 2a). The first step is to directly print the sacrificial 3D template in the shape of the desired channel network, such that the dimensions of the template can be carefully controlled and channels of considerable complexity can be easily formed. The second step is to cast the chip material around the template. We lower the template, still attached to the printing substrate, into a cavity containing a low-viscosity polymer precursor. The assembly is then photocured, encapsulating the template in a cross-linked polymer of well-defined, homogeneous refractive index and mechanical properties. In the third step, the template is dissolved away. The chip with the encapsulated template is removed from the printing substrate. The template is then dissolved by immersing the chip in water, which does not affect the cross-linked polymer.

While several materials can be used to print the template, our preferred material is the sugar alcohol isomalt, because it is insoluble in the prepolymer used to form the chip but is easily dissolved by water in the final step. A still image of the printing process is shown in Figure 2b, and a video of the template printing is provided in Supporting Information Movie 1. Though it is possible to print a helical template with any pitch greater than the channel radius, we chose a relatively large pitch of 500 μm , so that, in a transmission optical image, overlap between consecutive half-turns was limited. This facilitated measurement of the minor radius r in the nonoverlapping regions (Figure 2c, inset shows the mixing area magnified). The minor radius r was $78 \pm 1.8 \mu\text{m}$ over the 8.5 turns of the helix, and the major radius helix R was 313 μm . This R is 7.4% smaller than the diameter of the programmed deposition path and is caused by the constant radial acceleration of the nozzle, which pulls the small portion of the filament that is still molten

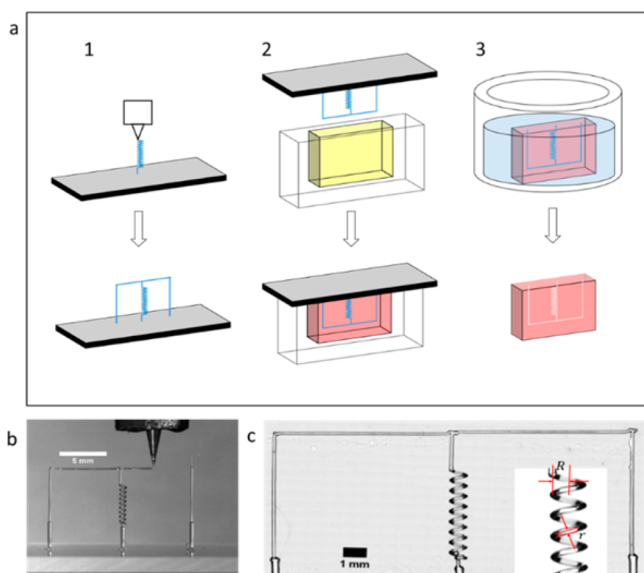


Figure 2. 3D printing for sacrificial monolithic microfluidic device formation. (a) The fabrication process consists of three steps. Step 1 is direct printing of a freestanding, 3D isomalt sacrificial template onto a substrate. In step 2, the template is inverted and placed in a silicone cavity containing a UV curable resin, which is cured by illuminating through the cavity to yield a monolithic block encapsulating the template. In step 3, the isomalt is dissolved out of the chip using water to yield a monolithic device with channels defined by the template. (b) Photograph during printing of the sacrificial template (video of the printing process is available as [Supporting Information Movie 1](#)). (c) White light optical image of the finished mixer, with the inset showing the helical mixer region and measures used to characterize the structure.

toward the center of the helix. The same effect is observed in other approaches to freeform printed helices.³⁹

Mixing Visualization. Confocal fluorescence microscopy has been used to visualize microfluidic mixing,^{3,4,40} but the technique presents an inherent problem for nonfluorescent species. Attaching a bulky fluorescent probe to a chemical can significantly change its physical, chemical, and transport properties in solvents. This makes tagging impractical for many systems, and impossible for those where the concentrations of small molecules or solvents are of interest. Our system, which comprises epoxy, glucose, NaCl, and water, is one such example—there is no inherent optical contrast between the components, and attaching an optical tag to glucose would be impractical and perturbative. However, these species have different chemical structures and, therefore, different vibrational spectra ([Figure 3a](#)). This makes Raman spectroscopic imaging ideal for directly quantifying the concentration of the nonionic components at any given point in the device. Glucose and saltwater show significant spectral differences in the 2700–3000 cm^{-1} region arising from the glucose C–H bonds, and so can be easily separated within the channel. While glucose and epoxy have overlapping spectral features, they are spatially separated (inside vs outside of the channel). SRS has good depth sectioning capabilities due to the inherent two-photon nature of the signal; hence, there is minimal signal overlap between the two compounds. Consequently, we can monitor the molecule of interest and, therefore, visualize the flows of the two liquid components in “one shot” with a single image taken at a Raman shift of 2894 cm^{-1} ([Figure 3b](#)).

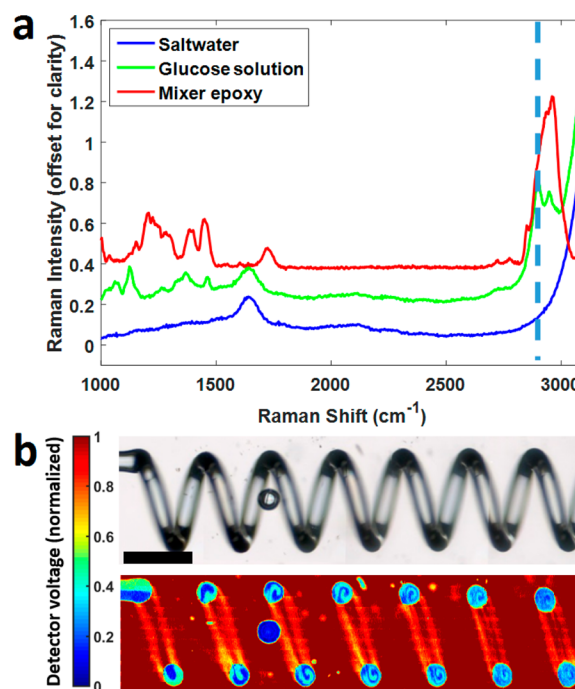


Figure 3. Raman spectroscopic characterization and imaging of the chemical constituents and mixers. (a) Spontaneous Raman spectra of saltwater, glucose solution, and the epoxy used to fabricate the mixer. A single frequency (2894 cm^{-1} , indicated with a dashed line) can be used to differentiate the two solutions within the channel while the epoxy is spatially distinct. (b) A white-light image of the helix and the corresponding stimulated Raman intensity image of a single spatial plane (or slice) through the center of the mixer. Channel cross sections are well resolved with clearly visible concentrations of the glucose solution. The scale bar indicates 500 μm .

The increase in information content in SRS images as compared to optical microscopy is apparent. Visualizing cross sections every 1/2 helix turn is readily accomplished by focusing the microscope objective to the center of the mixer and acquiring a single image along the entire length of the device. 3D images are acquired by z-stack imaging. ([Supporting Information Movie 2](#)). Because the intensity of the stimulated Raman scattering is linearly proportional to the glucose concentration, and the response of the photodiode detector is linearly proportional to the scattering intensity, the resulting image is quantitative. The signal intensity recorded from a uniform image of 0% glucose, 5.7% by weight salt solution was 0.17 V, and the signal intensity recorded from a uniform image of 8% by weight glucose solution was 0.42 V. Both signals had a standard deviation of 0.03 V. To quantify mixing, we linearly mapped the range 0.17 V to 0.42 V between 0 and 1. In order to characterize a more complex system, a sequence of images can probe multiple Raman shifts. While 3D images can provide visualizations throughout the entire device, a cross section of the circular area at various flow rates can illustrate the progression of mixing within the channel. [Figure 4](#) shows the glucose concentration at several cross sections as measured by SRS imaging and compares it to that predicted by computational modeling.

As expected for a laminar regime with a very controlled geometry, the agreement is excellent. Furthermore, the only experimental parameters used to generate the model were the optically measured major and minor radii, R and r , and the density and viscosity properties of saltwater and glucose

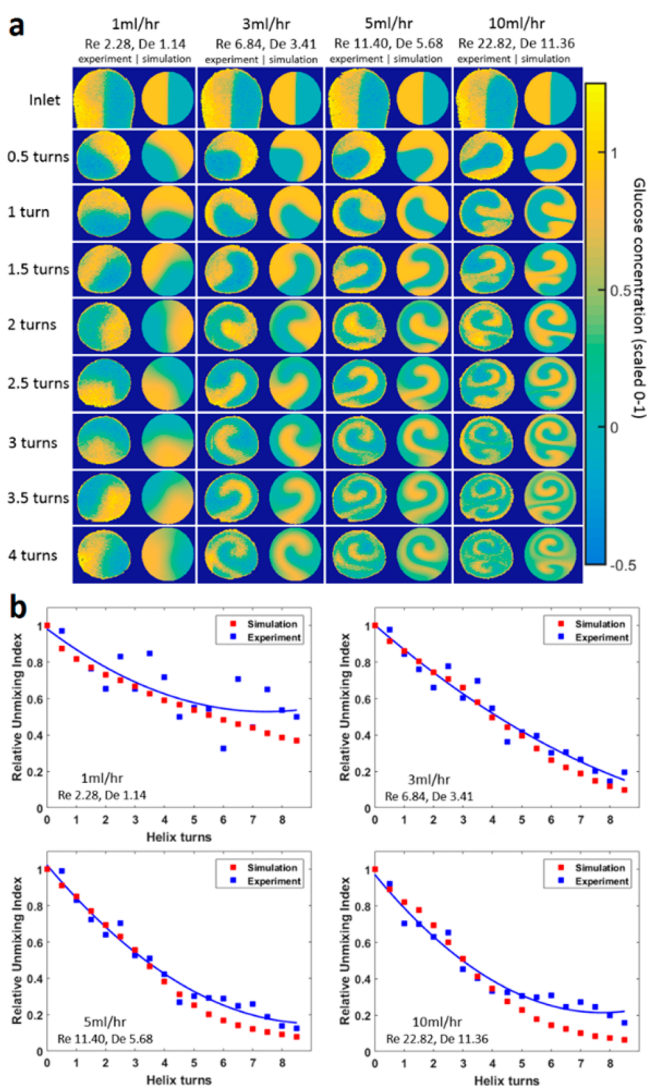


Figure 4. Theoretical and experimental comparisons of spatial concentration patterns and quantification of mixing along the channel. (a) Experimental (SRS) and simulation (COMSOL) visualizations of glucose concentration at cross sections in the helical mixer for four different flow rates (Reynolds and Dean numbers also shown). The SRS images have been scaled to show relative glucose concentration from 0 to 1, although pixels outside of this range appear due to noise. In the interest of space, only the first 4 turns are shown. (b) Relative unmixing index as calculated from these cross section images for experiment and simulation. Trend lines to the experiment are derived using the best fit for second order polynomials.

solutions as obtained from the literature. The simulated geometry was thus a perfectly helical pipe, and the inlet boundary condition was a symmetric distribution of the two input fluids such that their interface was parallel to the helical axis. This agreement attests to the fidelity of the printing process and shows that devices made in this way can be highly amenable to modeling and optimization prior to actual fabrication. For the experiments at higher De , there is deviation between the model and experiment due to an entrance effect which is not captured in the model's inlet boundary condition. Briefly, slight asymmetry in the T-junction where the inlet channels meet causes the interface of the two fluids to rotate slightly before it enters the helix. At these higher values of De , the mixing performance becomes strongly dependent on the

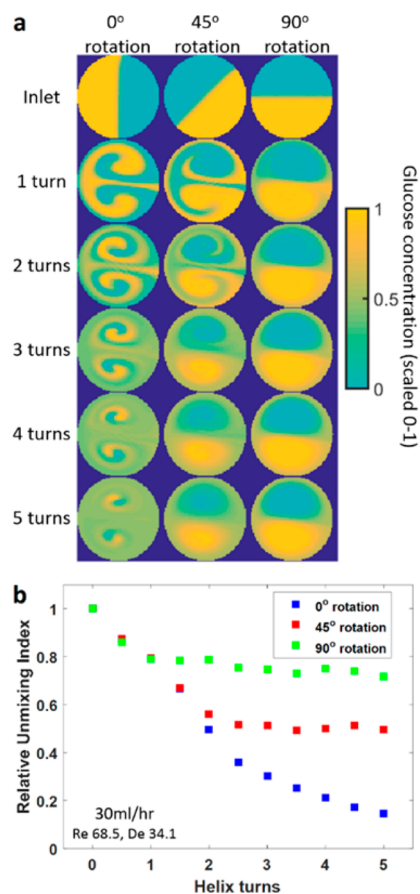


Figure 5. Effect of inlet rotation on mixing length. (a) COMSOL simulations of glucose concentration at cross sections in the helical mixer for three different inlet conditions at $De = 34.1$. (b) Relative unmixing index for each inlet condition along the length of the helix.

orientation of the fluid interface at the device inlet. Figure 5 demonstrates the effect of the inlet interface orientation on mixing.

Performance Analysis. To quantify the extent of mixing, we use the relative unmixing index, which is defined as the ratio of the standard deviation of the pixel intensities at a given cross section to the standard deviation at the inlet.⁴¹ This is mapped to a number between 0 and 1, where 0 represents perfect mixing and 1 no mixing. The evolution of the unmixing index along the length of our mixer is shown Figure 4b. The close correspondence between the experimental and theoretical predictions allows us to use numerical modeling to compare our helical mixer to existing standards of mixing in conventional microfluidics. For comparison, we use a scaled version of the optimized herringbone mixer design given by Ansari and Kim.⁴² We quantified mixer performance in terms of the volume, time, and pressure drop required to achieve a relative unmixing index of 0.15 (Figure 6). We scaled the dimensions of a simulated herringbone mixer such that the mixer volume and pressure drop were matched for the herringbone and 3D helical mixers at the same value of Re . This occurred at $Re \approx 10$. For $Re < 10$, the volume and pressure drop were lower for the herringbone mixer. For $Re > 10$, the volume and pressure drop were lower for the helical mixer. At all values of Re , the mixing time was lower for the helical mixer. Thus, for $Re > 10$, the simulated helix design outperforms the simulated herringbone design by all three metrics.

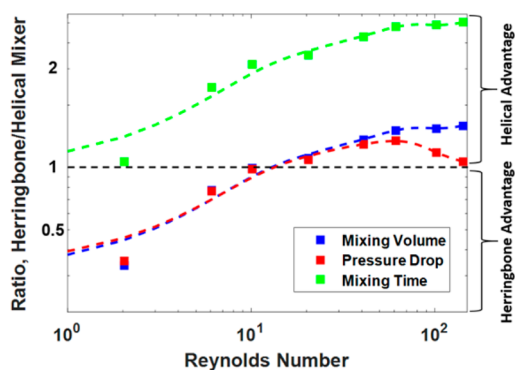


Figure 6. Relative performance of helical and herringbone mixers. Data points for mixing length, time, volume, and pressure drop are the ratio of the values required to obtain 85% mixing for the helical and herringbone devices. Above a Re of 10.2, the helical mixer requires less time, volume, and pressure to achieve this degree of mixing, and the ratio rises above 1 for all three metrics.

DISCUSSION

Aberration-free imaging is essential to quantitative characterization of microfluidic devices, including mixers. Mixing is a classical and ubiquitous problem in microfluidic devices;⁴³ though helical mixers have been fabricated in fused silica using femtosecond laser machining and HF etching,^{17,44,45} to our knowledge, their performance has not been well-validated. Our approach addresses this problem by simple 3D fabrication that allows facile matching of refractive indices,¹² an approach that has only been used in a few microfluidic studies.^{46–49} Our approach enables accurate imaging of the helical mixer, as evidenced by the close correspondence between the simulated and measured mixing profiles. At the higher values of De tested (faster fluid flow), entrance effects in the real mixer skew the inlet concentration profile so that it no longer matches the boundary condition specified in the simulation. Additionally, at these higher values of De , the flow profile also transitions from a single vortex to two vortices, with one vortex in the top half (closer to the inlet) of the cross section and another vortex in the bottom half (closer to the outlet). This flow pattern causes effective mixing within each half, but almost no mixing between the two halves. The result is that at high flow rates the mixing performance is far better in the model than in the experiment. This discrepancy underscores the value of being able to directly measure transport in microfluidics even in cases where the underlying physics are well understood. Even for relatively simple devices, a small error in the simulation inputs can lead to a large error in the simulation output.

Because microfluidic device fabrication via 3D freeform printing is a significant departure from more traditional methods, an extant need was to demonstrate that these devices are capable of performing at approximately the same level as established device designs. While the helical mixer was chosen due to its difficult-to-image geometry and interesting flow patterns, its performance was seen to be comparable to the gold standard staggered herringbone mixer. For $Re > 10$, the simulated helical mixer required less time, less volume, and a lower pressure drop to achieve a specified unmixing index than did the simulated herringbone mixer. The advantage of the helical mixer at higher Re is due in part to the circular channel cross section, which maximizes the hydraulic diameter and thus minimizes the pressure drop per unit length for a channel of given volume. If the mixer itself is the only microfluidic

component and the flow rate is relatively low, an inefficient mixer that requires a high input pressure may be acceptable; however, if multiple components are connected in series, the sum of the pressure drops may be high enough to cause bonded chips to delaminate and soft PDMS chips to deform.⁵⁰ Monolithic devices are immune to failure by delamination, and for devices made of low-stiffness materials, the lower pressure drop of a helical mixer at higher Re allows for high flow rates and placement of multiple components in series without risking deformation. For very-high-pressure applications, the monolithic casting approach can be used to make mixers with very thick walls, using very stiff materials. The ability to run chips at very high flow rates, coupled with the minimization of fouling in a round cross section, suggests utility in nanoparticle synthesis, where throughput and fouling have been cited as concerns.^{51,52} Thus, these round-channel devices may afford new opportunities in cases where conventional microfluidics fall short of current needs.

The ability to rapidly acquire quantitative 3D chemical images presents a new avenue for characterizing not only mixing, but other aspects of microfluidic device performance as well. Though we imaged only the effects of advection and diffusion, mass transport in microfluidics can also be caused by electrical, chemical, thermal, magnetic, or gravitational potential fields.⁵³ When these forces act on a small dissolved species, there may be no suitable probe that can be introduced without changing the behavior of the system. In these cases, SRS allows direct, label-free acquisition of 3D concentration maps for multiple analytes. Raman spectroscopy is also sensitive to the formation and destruction of chemical bonds, to adsorption,⁵⁴ and to conformational changes.⁵⁵ This is valuable in synthetic and analytical applications in which one needs to capture spatial heterogeneity within the chip, or when high acquisition speed is required. The demonstration of SRS imaging for quantifying mixing of a small molecule in solution therefore suggests further development for monitoring multiple components.

CONCLUSION

In this work, we demonstrated full 3D high-resolution imaging of flows within a complex microfluidic device. This was accomplished by two distinct means. First, a fabrication procedure via sacrificial molding of freeform 3D printed isomalt enables fine control over the optical properties of the device. This strategy allows for refractive index matching and the significant reduction of optical aberrations without adjusting the properties of the fluid. Second, in turn, we demonstrate that stimulated Raman scattering (SRS) microscopy can be used to directly visualize the concentration of different chemical components within the mixer, without the use of exogenous labels which cannot be attached to small molecules and may otherwise affect the behavior of relevant species. We investigated the effect of experimental parameters on mixing performance and show agreement between experimental results from SRS imaging and numerical solutions of theoretical models. These results demonstrate a versatile new manufacturing method for round-channel microfluidics, the ability to accurately simulate the behavior of such devices during the design phase, an efficient approach to mixing in such devices, and the utility of SRS as a fast, label-free means for characterizing the operation of microfluidic devices in general. The principles from this approach should pave the way for analysis of more complex monitoring in physiologically relevant

systems and for accurate spectroscopic monitoring of reactions in high-flow, low-fouling devices.

METHODS

Mixer Fabrication. The helical mixer was fabricated on a 3D printer developed in-house and using a similar process as described previously.³² A sacrificial template was designed in AutoCAD and printed on the freeform 3D printer using sugar alcohol isomalt (GalenIQ 990). The isomalt was heated to 115 °C and extruded through a 55 μm diameter nozzle translated directly along paths corresponding to the desired channel geometry. The extrusion pressure was 480 kPa, except for the input ports, for which the extrusion pressure was 1930 kPa. A video of the printing process is available as supplementary Movie 1. The printing speed was 0.2 mm/s and printing took about 6 min. A transparent silicone cavity was filled with a photocurable low-refractive-index prepolymer (MY-134, My Polymers, Nes Ziona, Israel). The sacrificial template was inverted and placed in the cavity, and the prepolymer was cured by illuminating both sides of the mold using a mercury lamp for 20 min. Upon release from the cavity, the isomalt was removed by leaving the device in water overnight at 90 °C.

Modeling. The mixing behavior of the glucose and NaCl solutions was modeled using the COMSOL Multiphysics Package (COMSOL Group, Stockholm, Sweden). The geometry of the model was a helix with the same major and minor radii as measured from an optical image of the device. The pitch and number of turns were the values corresponding to the programmed printer deposition path. The simulation solved the steady state, incompressible Navier–Stokes (NS) equation without the external force field for conservation of mass and momentum:

$$\nabla \cdot u = 0$$

$$\rho(u \cdot \nabla)u = \nabla^*[-pI + \mu(\nabla u + (\nabla u)^T)]$$

where u is the velocity, P is the pressure, ρ is the density, and μ is the viscosity of the fluid. The use of continuum mechanics is justified by calculation of the Knudsen number as less than 0.01.⁵⁶ In addition, the coupled convection-diffusion (CD) equation of a diluted species was used to model the transport of glucose and NaCl in water, tracking the location of the interface between two solutions:

$$\nabla \cdot (D\nabla c) + \mu \cdot \nabla c = 0$$

where c represents the relative concentration of the sodium and glucose solutions. The converged solution of NS was fed into CD with the velocity field, and the CD equation coupled back with the NS equation through the dependence of the density and viscosity on the relative concentration. We approximated the mixed fluid viscosity and density as a linear interpolation function between two solutions:

$$\mu = c\mu_1 + (1 - c)\mu_2$$

$$\rho = c\rho_1 + (1 - c)\rho_2$$

where the indices 1 and 2 stand for the sodium and glucose solutions, respectively. Values for viscosity, density, and the diffusion coefficient of 8% by weight glucose and 5.7% by weight NaCl in water were taken from the literature.^{57–60} We assumed that the mutual interaction between two solutions on diffusion coefficient is small enough not to affect the whole mixing behavior. The no-slip boundary condition on the walls

was applied, as is appropriate for microchannels of hydraulic diameter greater than 30 μm.⁶¹ We used several techniques to reduce the complexity of computational fluid modeling with μ -level resolution accuracy: 1) The NS and the CD equations were calculated separately to reduce the computational cost. 2) The computational domain in NS and CD equations was divided into two parts. For the first part of the domain, the inlet velocity and concentration profiles were specified, matching the experiment setup, and the passive outlet boundary condition ($p = 0$ for NS, or convective flux condition for CD) was applied. The velocity and concentration profiles at the outlet were exported, and imported as an inlet conditions for the second part of the domain to complete the results. 3) To improve the convergence of the simulation, the initial conditions of the high inlet volume flow rate cases were set through viscosity ramping, starting from higher viscosities (weakly nonlinear problem), and progressively increasing the nonlinearity until the original problem (highly nonlinear problem) is solved.

Modeling of the herringbone mixer was performed using the optimized design given in ref 42 with $W = 380 \mu\text{m}$, $d/h = 0.48$, and $\theta = 53.2^\circ$. The mixing time T , pressure drop P , and mixing volume V , were then determined for a mixer in which $W = 480 \mu\text{m}$ using the following relations:

$$\frac{T_2}{T_1} = \left(\frac{W_2}{W_1}\right)^2$$

$$\frac{P_2}{P_1} = \left(\frac{W_1}{W_2}\right)^2$$

$$\frac{V_2}{V_1} = \left(\frac{W_2}{W_1}\right)^3$$

These scaling relations are derived from the assumption that the mixing profile is purely a function of the Péclet number. $W_2/W_1 = 1.26$ was chosen so that the P and V curves for the helical mixer crossed the corresponding curves for the herringbone mixer at the same value of Re .

Stimulated Raman Imaging. All spectroscopic images were acquired using an SRS imaging microscope constructed in house. The SRS microscope is driven by a dual-output (1064 nm/532 nm) ultrafast oscillator coupled into an optical parametric oscillator to provide two picosecond pulse trains whose wavelength difference can be tuned to match a Raman mode of interest. The imaging was performed using a long working distance near-infrared-corrected objective and a custom-built single-element photodiode detector. A pair of galvanometer mirrors was used to scan the focused beams across the specimen during acquisition. For measuring channel cross sections, we chose a pixel size of 2 μm to be sufficient for clearly resolving the internal structure. For 3D images of the full mixer acquired via z-stack, we chose a cubic voxel of 5 μm on a side.

Image Processing. All images were processed in Matlab (The Mathworks, Nantucket, MA). Briefly, the Raman signal from the epoxy is used as an internal standard to account for any nonuniformity in image intensity due to laser fluctuation or imaging depth. As the epoxy provides the strongest signal, it can be readily masked out, leaving only the channel cross sections. The image intensity of each set of cross sections was scaled so that the saltwater solution at the mixer input had an average value of 0 and the glucose solution at the mixer input

had an average value of 1. In order to compare simulation results to experimental images, the simulation meshes were mapped onto a square grid of effective pixel size $2 \mu\text{m}$. Additionally, the SRS images contain a noise component which the simulation results do not, and this value was taken into consideration when extracting performance metrics from the experimental data. The relative unmixing index I is given by

$$I = \sqrt{\frac{\frac{1}{N} \sum_{j=1}^N (x_j - \bar{x}_j)^2}{\frac{1}{N} \sum_{i=1}^N (x_i - \bar{x}_i)^2}}$$

where x_i are the pixel intensities at the inlet and x_j the pixel intensities at the cross section of interest. We correct for the noise in the image by subtracting the variance due to noise σ_n^2 from the total variance at each cross section:

$$I = \sqrt{\frac{\frac{1}{N} \sum_{j=1}^N (x_j - \bar{x}_j)^2 - \sigma_n^2}{\frac{1}{N} \sum_{i=1}^N (x_i - \bar{x}_i)^2 - \sigma_n^2}}$$

■ ASSOCIATED CONTENT

📄 Supporting Information

The Supporting Information is available free of charge on the ACS Publications website at DOI: 10.1021/acs.analchem.6b03943.

Figure showing the theoretical and experimental comparisons of spatial concentration patterns and quantification of mixing along the channel at higher flow rates (PDF)

Video showing 3D printing of a sacrificial mold (MPG)

Video showing a z-stack through the mixing chip (MPG)

■ AUTHOR INFORMATION

Corresponding Author

*E-mail: rxb@illinois.edu.

ORCID

Rohit Bhargava: 0000-0001-7360-994X

Notes

The authors declare no competing financial interest.

■ ACKNOWLEDGMENTS

We gratefully acknowledge the support of the Beckman Institute for Advanced Science and Technology via a seed grant for development of the 3D printer. We gratefully acknowledge the gift of isomalt and advice on its processing provided by Oliver Luhn of Suedzucker AG/BENEOPalatin GmbH. The development of SRS imaging methods was supported by NIH via Grants R21CA190120 and R01CA197516.

■ REFERENCES

- (1) Whitesides, G. M. *Nature* **2006**, *442*, 368–373.
- (2) Xi, C.; Marks, D. L.; Parikh, D. S.; Raskin, L.; Boppart, S. A. *Proc. Natl. Acad. Sci. U. S. A.* **2004**, *101*, 7516–7521.
- (3) Ismagilov, R. F.; Stroock, A. D.; Kenis, P. J. A.; Whitesides, G.; Stone, H. A. *Appl. Phys. Lett.* **2000**, *76*, 2376–2378.
- (4) Park, T.; Lee, M.; Choo, J.; Kim, Y. S.; Lee, E. K.; Kim, D. J.; Lee, S. H. *Appl. Spectrosc.* **2004**, *58*, 1172–1179.
- (5) Schafer, D.; Gibson, E. A.; Amir, W.; Erikson, R.; Lawrence, J.; Vestad, T.; Squier, J.; Jimenez, R.; Marr, D. W. *Opt. Lett.* **2007**, *32*, 2568–2570.

- (6) Salmon, J.-B.; Ajdari, A.; Tabeling, P.; Servant, L.; Talaga, D.; Joanicot, M. *Appl. Phys. Lett.* **2005**, *86*, 094106.
- (7) Schafer, D.; Squier, J. A.; Maarseveen, J. v.; Bonn, D.; Bonn, M.; Müller, M. *J. Am. Chem. Soc.* **2008**, *130*, 11592–11593.
- (8) Schafer, D.; Müller, M.; Bonn, M.; Marr, D. W. M.; van Maarseveen, J.; Squier, J. *Opt. Lett.* **2009**, *34*, 211–213.
- (9) Min, W.; Freudiger, C. W.; Lu, S.; Xie, X. S. *Annu. Rev. Phys. Chem.* **2011**, *62*, 507–530.
- (10) Wiedersheimer, S.; Andreini, N.; Epely-Chauvin, G.; Ancey, C. *Exp. Fluids* **2011**, *50*, 1183–1206.
- (11) Li, S.; Liu, J.; Nguyen, N.-T.; Fang, Z. P.; Yoon, S. F. *Appl. Opt.* **2009**, *48*, 6432–6441.
- (12) Budwig, R. *Exp. Fluids* **1994**, *17*, 350–355.
- (13) Besseling, T. H.; Jose, J.; BLAADEREN, A. *J. Microsc.* **2015**, *257*, 142–150.
- (14) Stroock, A. D.; Dertinger, S. K. W.; Ajdari, A.; Mezić, I.; Stone, H. A.; Whitesides, G. M. *Science* **2002**, *295*, 647–651.
- (15) Sudarsan, A. P.; Ugaz, V. M. *Proc. Natl. Acad. Sci. U. S. A.* **2006**, *103*, 7228–7233.
- (16) Liu, K.; Yang, Q.; He, S.; Chen, F.; Zhao, Y.; Fan, X.; Li, L.; Shan, C.; Bian, H. *Microsyst. Technol.* **2013**, *19*, 1033–1040.
- (17) Liu, K.; Yang, Q.; Chen, F.; Zhao, Y.; Meng, X.; Shan, C.; Li, Y. *Microfluid. Nanofluid.* **2015**, *19*, 169–180.
- (18) Stevenson, W. H.; Thompson, H. D.; Durrett, R. P.; Gould, R. D. *AIAA J.* **1985**, *23*, 1387–1391.
- (19) Sackmann, E. K.; Fulton, A. L.; Beebe, D. J. *Nature* **2014**, *507*, 181–189.
- (20) Unger, M. A.; Chou, H. P.; Thorsen, T.; Scherer, A.; Quake, S. R. *Science* **2000**, *288*, 113–116.
- (21) Huang, Z.; Li, X.; Martins-Green, M.; Liu, Y. *Biomed. Microdevices* **2012**, *14*, 873–883.
- (22) Fiddes, L. K.; Raz, N.; Srigunapalan, S.; Tumarkan, E.; Simmons, C. A.; Wheeler, A. R.; Kumacheva, E. *Biomaterials* **2010**, *31*, 3459–3464.
- (23) Yang, X.; Forouzan, O.; Burns, J. M.; Shevkoplyas, S. S. *Lab Chip* **2011**, *11*, 3231–3240.
- (24) Bischel, L. L.; Young, E. W.; Mader, B. R.; Beebe, D. J. *Biomaterials* **2013**, *34*, 1471–1477.
- (25) Bischel, L. L.; Beebe, D. J.; Sung, K. E. *BMC Cancer* **2015**, *15*, 12.
- (26) Dolega, M. E.; Wagh, J.; Gerbaud, S.; Kermarrec, F.; Alcaraz, J. P.; Martin, D. K.; Gidrol, X.; Piccollet-D'hahan, N. *PLoS One* **2014**, *9*, e99416.
- (27) Mohammadi, M.; Sharp, K. V. *J. Fluids Eng.* **2015**, *137*, 0312081–0312087.
- (28) Miller, J. S.; Stevens, K. R.; Yang, M. T.; Baker, B. M.; Nguyen, D.-H. T.; Cohen, D. M.; Toro, E.; Chen, A. A.; Galie, P. A.; Yu, X.; Chaturvedi, R.; Bhatia, S. N.; Chen, C. S. *Nat. Mater.* **2012**, *11*, 768–774.
- (29) Toohey, K. S.; Sottos, N. R.; Lewis, J. A.; Moore, J. S.; White, S. R. *Nat. Mater.* **2007**, *6*, 581–585.
- (30) Theriault, D.; White, S. R.; Lewis, J. A. *Nat. Mater.* **2003**, *2*, 265–271.
- (31) Wu, W.; Hansen, C. J.; Aragon, A. M.; Geubelle, P. H.; White, S. R.; Lewis, J. A. *Soft Matter* **2010**, *6*, 739–742.
- (32) Gelber, M. K.; Bhargava, R. *Lab Chip* **2015**, *15*, 1736–1741.
- (33) He, Y.; Qiu, J.; Fu, J.; Zhang, J.; Ren, Y.; Liu, A. *Microfluid. Nanofluid.* **2015**, *19*, 1–10.
- (34) Howell, J. P. B.; Mott, D. R.; Golden, J. P.; Ligler, F. S. *Lab Chip* **2004**, *4*, 663–669.
- (35) Schönfeld, F.; Hardt, S. *AIChE J.* **2004**, *50*, 771–778.
- (36) Kumar, V.; Aggarwal, M.; Nigam, K. D. P. *Chem. Eng. Sci.* **2006**, *61*, 5742–5753.
- (37) Cookson, A. N.; Doorly, D. J.; Sherwin, S. J. *Ann. Biomed. Eng.* **2009**, *37*, 710–721.
- (38) Verma, M. K.; Ganneboyina, S. R.; R, V. R.; Ghatak, A. *Langmuir* **2008**, *24*, 2248–2251.
- (39) Farahani, R. D.; Chizari, K.; Theriault, D. *Nanoscale* **2014**, *6*, 10470–10485.

- (40) Zeng, Y.; Jiang, L.; Zheng, W.; Li, D.; Yao, S.; Qu, J. Y. *Opt. Lett.* **2011**, *36*, 2236–2238.
- (41) Hashmi, A.; Xu, J. *J. Lab. Autom.* **2014**, *19*, 488–491.
- (42) Ansari, M. A.; Kim, K. Y. *Chem. Eng. Sci.* **2007**, *62*, 6687–6695.
- (43) Lee, C.-Y.; Chang, C.-L.; Wang, Y.-N.; Fu, L.-M. *Int. J. Mol. Sci.* **2011**, *12*, 3263–3287.
- (44) Yang, J.; Qi, L.; Chen, Y.; Ma, H.; Chin, J. *Chin. J. Chem.* **2013**, *31*, 209–214.
- (45) Liao, Y.; Song, J.; Li, E.; Luo, Y.; Shen, Y.; Chen, D.; Cheng, Y.; Xu, Z.; Sugioka, K.; Midorikawa, K. *Lab Chip* **2012**, *12*, 746–749.
- (46) Wiederoder, M. S.; Peterken, L.; Lu, A. X.; Rahmanian, O. D.; Raghavan, S. R.; DeVoe, D. L. *Analyst* **2015**, *140*, 5724–5731.
- (47) Blois, G.; Barros, J. M.; Christensen, K. T. In PIV13; 10th International Symposium on Particle Image Velocimetry, Delft, The Netherlands, July 1–3, 2013; Delft University of Technology, Faculty of Mechanical, Maritime and Materials Engineering, and Faculty of Aerospace Engineering, 2013.
- (48) Thomas Levario, P. I.; Hyundoo, H.; Shai, S.; Hang, L. In Proceedings of Micro Total Analysis Systems 2014 Conference: San Antonio, TX, U.S.A., 2014.
- (49) Zerai, B.; Saylor, B. Z.; Kadambi, J. R.; Oliver, M. J.; Mazaheri, A. R.; Ahmadi, G.; Bromhal, G. S.; Smith, D. H. *Transp. Porous Media* **2005**, *60*, 159–181.
- (50) Inglis, D. W. *Biomicrofluidics* **2010**, *4*, 026504.
- (51) Lohse, S. E.; Eller, J. R.; Sivapalan, S. T.; Plews, M. R.; Murphy, C. J. *ACS Nano* **2013**, *7*, 4135–4150.
- (52) Valencia, P. M.; Farokhzad, O. C.; Karnik, R.; Langer, R. *Nat. Nanotechnol.* **2012**, *7*, 623–629.
- (53) Panigrahi, P. K. In *Transport Phenomena in Microfluidic Systems*; John Wiley & Sons Singapore Pte. Ltd: 2016; pp 51–100.
- (54) Nie, S.; Emory, S. R. *Science* **1997**, *275*, 1102–1106.
- (55) Krimm, S.; Bandekar, J. In *Adv. Protein Chem.*; C.B. Anfinsen, J. T. E.; Frederic, M. R., Eds.; Academic Press: 1986; pp 181–364.
- (56) Gad-el-Hak, M. *J. Fluids Eng.* **1999**, *121*, 5–33.
- (57) Comesaña, J. F.; Otero, J. J.; García, E.; Correa, A. *J. Chem. Eng. Data* **2003**, *48*, 362–366.
- (58) Chang, Y.; Myerson, A. *AIChE J.* **1985**, *31*, 890–894.
- (59) Vitagliano, V.; Lyons, P. *J. Am. Chem. Soc.* **1956**, *78*, 1549–1552.
- (60) Gladden, J.; Dole, M. *J. Am. Chem. Soc.* **1953**, *75*, 3900–3904.
- (61) Zhu, L.; Tretheway, D.; Petzold, L.; Meinhart, C. J. *J. Comput. Phys.* **2005**, *202*, 181–195.